

## Microstructure, Anisotropy and Formability Evolution of an Annealed AISI 430 Stainless Steel Sheet

Iquilio Abarzúa, Roberto; Hernández-Durán, Eliseo; Nguyen-Minh, Tuan; Kestens, Leo A.I.; Valín Rivera, José Luis; Castro Cerda, Felipe M.

**DOI**

[10.1002/srin.202100114](https://doi.org/10.1002/srin.202100114)

**Publication date**

2021

**Document Version**

Final published version

**Published in**

Steel Research International

**Citation (APA)**

Iquilio Abarzúa, R., Hernández-Durán, E., Nguyen-Minh, T., Kestens, L. A. I., Valín Rivera, J. L., & Castro Cerda, F. M. (2021). Microstructure, Anisotropy and Formability Evolution of an Annealed AISI 430 Stainless Steel Sheet. *Steel Research International*, 93(1), Article 2100114. <https://doi.org/10.1002/srin.202100114>

**Important note**

To cite this publication, please use the final published version (if applicable). Please check the document version above.

**Copyright**

Other than for strictly personal use, it is not permitted to download, forward or distribute the text or part of it, without the consent of the author(s) and/or copyright holder(s), unless the work is under an open content license such as Creative Commons.

**Takedown policy**

Please contact us and provide details if you believe this document breaches copyrights. We will remove access to the work immediately and investigate your claim.

# Microstructure, Anisotropy and Formability Evolution of an Annealed AISI 430 Stainless Steel Sheet

Roberto Iquilio Abarzúa,\* Eliseo Hernández-Durán, Tuan Nguyen-Minh, Leo A. I. Kestens, José Luis Valín Rivera, and Felipe M. Castro Cerda

The effect of the microstructure on the principal strain paths (uniaxial, plane, and biaxial) in the formability processes of ferritic stainless steel AISI 430 sheets is studied. The Marciniak test (determination of the plastic strain of sheet metal with a flat tip punch) is applied to determine the forming limit curves and different strain levels in the strain paths by the digital image correlation technique. The formability is discussed in light of the microstructure, standard mechanical properties, work hardening behavior, and anisotropy measurements (*R*-value). Electron backscatter diffraction analysis is carried out to determine the texture of the selected strain paths. The texture evolution shows a marked  $\gamma$  ( $\langle 111 \rangle //$  normal direction [ND]) fiber and cube ( $\{001\} \langle 100 \rangle$ ) texture component under the biaxial strain mode, whereas the  $\alpha$  ( $\langle 110 \rangle //$  rolling direction [RD]) fiber is somewhat favored under uniaxial plane strain. The results are compared with texture simulations performed under the fully constrained Taylor model, finding reasonable agreement with the experimentally measured main components.

## 1. Introduction

Stainless steel represents a large family of iron-based alloys of which the principal characteristic is its good corrosion resistance. Nowadays, ferritic stainless steels (FSSs) are widely accepted for use in a wide variety of applications, as, for example, structural framework and body panels for buses and cars,<sup>[1]</sup> not to mention

that it is much cheaper than 300 series stainless steels. One of its disadvantages is that it is more susceptible to corrosion than the 300 series grades because its main alloying element is chromium.<sup>[2]</sup> The FSS has an excellent resistance to stress corrosion cracks, pitting, and crevice-type of corruptions. Furthermore, this stainless-steel grade shows a low strain hardening rate, which allows them to be easily deformed by any metal working process.

Steels are strengthened by various possible mechanisms of hardening. Hardening by plastic deformation is one of the most important methods of strengthening metals. When a crystalline solid is deformed plastically, it becomes more resistant, and a greater stress is required for additional deformation.<sup>[3]</sup> The hardening in a crystalline structure occurs because these materials

deform plastically by the movement of dislocations. When a polycrystal is deformed in rolling, forming, drawing, and so on, the randomly oriented grains will slip on their appropriate glide systems and rotate from their initial conditions, under the constraint from the neighboring grains.<sup>[3]</sup> This leads to a strong increase in dislocation density, which in turn produces a higher yield strength. Dislocation sources create new dislocations during plastic deformation and serve to increase the dislocation density. This hardens the material, a process called work hardening, strain hardening, or sometimes strengthening by cold working.<sup>[4]</sup>

The formability test is a widely applied technique used in the manufacturing of metal sheet parts. The formability process includes a variety of types and operating conditions. An important tool used to evaluate the formability of metal sheets is the forming limit diagram (FLD). The FLD concept was introduced by Keeler and Backofen<sup>[5]</sup> and Goodwin.<sup>[6]</sup> The FLD represents the maximum values of the principal strains (major  $\epsilon_1$  and minor  $\epsilon_2$ ) that one metal sheet can withstand before the onset of necking. Currently, there are many different mechanical tests to determine the experimental FLD. Among these, the most commonly used tests are the Marciniak<sup>[7]</sup> and Nakazima<sup>[8]</sup> tests, whereby the sheet metal is plastically strained by a flat tip or a round-tip punch, respectively.<sup>[9]</sup> Both tests use different sample geometries to induce the different strain paths, whereby the principal difference is the punch geometry (see Appendix A).


Various approaches are used to determine the onset of necking and the corresponding limit strain. In one approach, grid circles and square patterns are applied on the sample, as proposed by

R. Iquilio Abarzúa, E. Hernández-Durán, F. M. Castro Cerda  
Departamento de Ingeniería Metalúrgica  
Universidad de Santiago de Chile  
Av. Lib. B. O'Higgins 3363, Estación Central, Santiago, Chile  
E-mail: roberto.iquilioa@usach.cl

J. L. Valín Rivera  
Escuela de Ingeniería Mecánica  
Pontificia Universidad Católica de Valparaíso  
Av. Brasil 2950, Valparaíso, Chile

E. Hernández-Durán, T. Nguyen-Minh, L. A. I. Kestens  
Department of Electromechanical  
System and Metal Engineering  
Tech Lane Ghent Science Park  
Campus A, Technologiepark 46, Zwijnaarde B9052, Belgium

E. Hernández-Durán, L. A. I. Kestens, F. M. Castro Cerda  
Department of Materials Science and Engineering  
Delft University of Technology  
Mekelweg 2, Delft 2628CD, The Netherlands

 The ORCID identification number(s) for the author(s) of this article can be found under <https://doi.org/10.1002/srin.202100114>.

DOI: 10.1002/srin.202100114

Keeler et al.<sup>[10]</sup> and Sowerby et al.,<sup>[11]</sup> respectively. Bragard et al.<sup>[12]</sup> developed a method with a grid of circles, whereby each test piece produces one single point in the FLD. The technique called digital image correlation (DIC) has been developed. DIC is a complete optical technique that allows gauging the displacement of a set of reference points on the entire sample surface. Different methods have been used to determine the limit strain and the FLD based on the DIC measurements of the position (stationary),<sup>[8]</sup> strain rate,<sup>[13–19]</sup> and strain acceleration<sup>[20]</sup> (time dependent) using the Hencky strain tensor. Furthermore, some researchers have presented methods that analyze thickness strain<sup>[21–23]</sup> and are capable of analyzing multiple local necks.<sup>[24,25]</sup>

There are a variety of parameters that influence the limit strain for the different strain paths, such as strain hardening ( $n$ ),<sup>[26]</sup> plastic anisotropy ( $R$ ),<sup>[26,27]</sup> strain rate hardening ( $m$ ),<sup>[26,28]</sup> strain path changes,<sup>[29]</sup> and strain homogeneity across the sheet thickness.<sup>[30]</sup> The crystallographic texture is one of the dominant microstructural characteristics that is of crucial importance for mechanical properties such as normal and planar plastic anisotropy or yield stress anisotropy. In rolling body-centered cubic materials (BCCs),  $\alpha$  fiber  $\langle 110 \rangle //$  rolling direction (RD),  $\gamma$  fiber  $\langle 111 \rangle //$  normal direction (ND), and  $\epsilon$  fiber  $\langle 110 \rangle //$  transverse direction (TD) represent the most common texture components. A number of studies on the influence of texture on formability properties have focused on texture evolution,<sup>[31]</sup> strain paths,<sup>[32]</sup> localized necking,<sup>[33]</sup> effects of friction on texture,<sup>[34]</sup> texture influence on anisotropy,<sup>[35]</sup> effects on cube texture, and different records of nonproportional loads.<sup>[36]</sup> None of the former investigations considered the microstructure and texture changes on annealed AISI 430 stainless steel under different strain paths.

The Taylor theory<sup>[37]</sup> and the full constraint Taylor model (FCTM) approach<sup>[38]</sup> have been thoroughly described in previous studies.<sup>[39,40]</sup> The essence of the FCTM is that macroscopically imposed strain is equal to the microscopic strain at crystallographic level. To apply the FCTM, the experimental textures by electron backscatter diffraction (EBSD) were converted to a continuous ODF and subsequently discretized according to a method proposed by Toth and Van Houtte.<sup>[41]</sup> The distribution of Taylor factors ( $M$ ) in the  $\varphi_2 = 45^\circ$  section of Euler space were calculated considering only the  $\{110\} \langle 111 \rangle$  and  $\{112\} \langle 111 \rangle$  slip systems, whereby the critical resolved shear stress on all 24 slip systems were considered to be identical. The total number of experimentally measured points is reduced, according to the method by Toth and Van Houtte,<sup>[41]</sup> to a set of 10 000 equally weighted orientations.

There is a lot of research on FSSs, however in the literature, there is a very low amount of research on the formability of these steels. Due to the wide use of AISI 430 steels, its good mechanical and formability properties, and their low cost compared to 300 series stainless steels, a study of the microstructural evolution, mechanical properties and deformation capacity is necessary.

In the present work, a detailed microstructure and formability analysis of AISI 430 stainless steel was carried out. Texture evolution and grain boundary misorientation development during straining under three different strain paths before the onset of necking were analyzed using EBSD. Texture analysis was performed to provide a better understanding of the anisotropy and formability in the studied steel. Furthermore, the texture evolution has been accounted for by performing simulations with the full-constraint Taylor crystal plasticity model. Through this study,

it was possible to analyze the influence of microstructural changes on both the mechanical and the formability properties.

## 2. Experimental Section

The studied material was a 1.2 mm-thick metal sheet made of commercial AISI 430 stainless steel with the chemical composition shown in Table 1. More details about the microstructural characterization of the as-received material can be found in the study by Iquilio et al.<sup>[25]</sup>

### 2.1. Microstructural Characterization

The preparation of the samples included standard processes of cutting, grinding, polishing, and etching. Mechanical grinding was performed manually using different grades of silicon carbide emery paper. The metallographic observation was performed in the plane spanned by the RD and ND.

EBSD characterization was performed with FEI Quanta 450-FEG-SEM system operated at 20 kV, with a beam current corresponding to a spot size of 5 for a 30  $\mu\text{m}$  aperture size (2.3 nA) and a working distance of 16 mm. The sample was tilted  $70^\circ$  to the horizontal axis of the microscope stage, and the EBSD patterns were acquired on a hexagonal scan grid with a Hikari detector operated with EDAX-TSL-OIM-Data Collection (version 6) software. The step size of the scans was 1.5  $\mu\text{m}$ . The orientation distribution functions (ODFs) were calculated by the spherical harmonic series expansion developed by Bunge.<sup>[42]</sup> The ODFs were derived from the EBSD scans by superimposing Gaussian distributions with a half width of  $5^\circ$ . The resulting ODF was represented as a series expansion of spherical harmonic functions with a maximum rank of the expansion coefficient  $L = 16$ . Each texture calculation is based on merging three scans with  $\approx 1 \text{ mm}^2$  areas with  $\approx 8.000$  single grains each. The raw EBSD data were postprocessed (cleaned) to reassign the incorrectly indexed points using the grain confidence index standardization procedure. The grains were defined as the arrangement of at least four points with a misorientation angle less than  $5^\circ$  and a confidence index  $> 0.1$ .

Furthermore, misorientation analysis by grain boundary misorientations was carried out. Microstructural analyses were carried out for the initial material (undeformed) and for the samples with different strain levels in uniaxial strain (US), plane strain (PS), and biaxial strain (BS) paths.

### 2.2. Tensile Test

The ASTM E8 standard was followed for tensile characterization. The tensile tests were carried out with three specimens for each direction at  $0^\circ$ ,  $45^\circ$ , and  $90^\circ$  with respect to the RD. The samples were sized to a gauge length of 50 mm and a width of 12.5 mm in the gauge section according to the standard. The tests were performed on a TINIUS&OLSEN universal tensile testing machine

**Table 1.** Chemical composition of the steel in wt.%.

Element	C	Mn	P	S	Si	Cr	Ni	Fe
Wt%	0.042	0.52	0.0099	0.0058	0.248	16.81	0.095	Rest.

with a 30 ton maximum capacity. The test samples were loaded under displacement control at a grip speed of  $2.5 \text{ mm min}^{-1}$  ( $\approx 10^{-3} \text{ s}^{-1}$ ).

The Lankford coefficients ( $R$ -value) were determined through tensile tests according to the ASTM E517 standard [43] at  $\approx 15\%$  engineering strain for each direction ( $0^\circ$ ,  $45^\circ$ , and  $90^\circ$ ). The tests were performed in duplicate at a cross-head displacement rate of  $0.5 \text{ mm min}^{-1}$  ( $\approx 10^{-4} \text{ s}^{-1}$ ). The  $R$ -values were obtained from the measurement of values in transverse and longitudinal lines using DIC.  $R$ -values were obtained from the average of the values contained in a line within a homogeneous deformation zone in both the major and the minor strain directions.

### 2.3. Formability Test

The Marciniak tests were performed according to the ISO 12004-2 standard [9] with a 100 mm-diameter flat punch with an edge radius of 10 mm. The Marciniak test equipment was mounted on the universal tensile test machine according to a previous study. [25] The tests were run at a crosshead speed of  $2.5 \text{ mm min}^{-1}$ , and the complete test surface up to fracture was recorded by obtaining full HD video from which images were extracted every 0.1 s. To avoid direct interaction between the punch and the sheet metal, an 85–15 brass mask with an outer diameter of 200 mm and internal diameter of 36 mm was fit between the punch and the specimens. To reduce friction between the punch and the mask, a sheet of 0.4 mm-thick polytetrafluoroethylene (Teflon) and a layer of molybdenum-based spray lubricant were used.

A Marciniak test was carried out for eight different geometric dimensions in the sheet for three directions with respect to the RD: the RD ( $0^\circ$ ), diagonal direction ( $45^\circ$ ), and transverse direction ( $90^\circ$ ) (see Appendix A). The forming limit curves (FLC) were constructed with the average true strain (Hencky) values of the three samples by geometry according to a previous study. [25] Two strain percentages were tested for US, PS, and balanced BS before the onset of necking.

True strains were measured using DIC with VIC-2D commercial software. The DIC analysis was carried out with an analysis window size of  $31 \times 31$  pixels. A speckled pattern was applied to the surface of each test specimen (surface treatment with white base paint and black point paint was applied randomly). The images with the speckled pattern were calibrated with zero-normalized cross correlation.

### 2.4. Texture Simulation

A full constraint Taylor (FCT) model was used to obtain the texture evolution under three different strain paths. For

simulations, the textures measured by EBSD were discretized into 10,000 discrete orientations, and  $\{110\} \langle 111 \rangle$  and  $\{112\} \langle 111 \rangle$  were considered the active slip systems. The hardening behavior of these two slip systems was assumed to be linear from the same initial critical resolved shear stress. Of all possible combinations of slips that can accommodate the prescribed strain, those that minimize internal work were chosen. The low-strain texture simulation results were not presented in this work due to the low level of effective strain applied in each of the three strain paths. The equivalent strain was amplified in the simulations to emphasize the effect on texture evolution. The applied equivalent strain in the three strain paths was  $\epsilon_{\text{eff}} = 0.41185$ .

The effective strain values were determined using Von Mises criterion according to

$$\epsilon_{\text{eq}} = \frac{2}{3} \sqrt{\frac{3(\epsilon_{xx}^2 + \epsilon_{yy}^2 + \epsilon_{zz}^2)}{2} + \frac{3(\gamma_{xy}^2 + \gamma_{yz}^2 + \gamma_{zx}^2)}{4}} \quad (1)$$

With the deviatoric strain

$$\epsilon_{xx} = +\frac{2}{3}\epsilon_{xx} - \frac{1}{3}\epsilon_{yy} - \frac{1}{3}\epsilon_{zz} \quad (2)$$

$$\epsilon_{yy} = -\frac{1}{3}\epsilon_{xx} + \frac{2}{3}\epsilon_{yy} - \frac{1}{3}\epsilon_{zz} \quad (3)$$

$$\epsilon_{zz} = -\frac{1}{3}\epsilon_{xx} - \frac{1}{3}\epsilon_{yy} + \frac{2}{3}\epsilon_{zz} \quad (4)$$

The engineering strain  $\gamma$  is defined as

$$\gamma_{ij} = 2 \times \epsilon_{ij} \quad (5)$$

## 3. Results

### 3.1. Mechanical Properties

The mechanical properties of the material are shown in **Table 2**: the load direction parallel to the RD, yield stress  $Y_S$ , ultimate tensile stress  $S_u$ , elongation at fracture  $E_l$ , coefficient of strain hardening  $n$ , and coefficient of resistance  $k$ , corresponding to the power law  $\sigma = k\epsilon^n$ . These data were obtained through the stress–strain curve between the yield stress and the ultimate tensile stress on the engineering stress–strain curve, except for the fitting with the power law, for which true values were used. The calculated  $R$ -values and normal and planar anisotropy are shown in **Table 3**.

**Table 2.** Tensile properties.

Sample orientation [°]	$Y_{S(0.2\%)} \text{ (SD) [Mpa]}$	$S_u \text{ (SD) [Mpa]}$	$E_l \text{ (SD) [\%]}$	$n \text{ (SD)}$	$k \text{ (SD) [Mpa]}$
$0^\circ$	271 (2.12)	373 (1.13)	29.1 (0.18)	0.19 (0.010)	621 (7.65)
$45^\circ$	291 (2.82)	393 (5.65)	28.0 (0.96)	0.18 (0.006)	651 (16.3)
$90^\circ$	284 (7.42)	389 (0.99)	27.6 (0.04)	0.18 (0.002)	638 (1.34)
X	282	385	28.2	0.18	636

**Table 3.** Anisotropy coefficients.

$R_0$	$R_{45}$	$R_{90}$	$\bar{R}$	$\Delta R$
0.91	0.58	1.48	0.89	0.61

### 3.2. Formability Evaluation

The FLC results are shown in **Figure 1a–c**, in which each of the FLCs corresponds to the three directions previously mentioned, considering  $\rho = \varepsilon_2/\varepsilon_1$  as the reference line of the strain path, where  $\rho = -0.5$  is the US path,  $\rho = 0$  is the PS path, and  $\rho = 1$  is the balanced BS path. Under the US condition, the highest values of the major strain are equal to  $\varepsilon_1 = 0.37$  for both the  $0^\circ$  and  $90^\circ$  directions, and the lowest value of  $\varepsilon_1 = 0.30$  is in the  $45^\circ$  direction. In the case of minor strain, the highest value is observed for the  $90^\circ$  direction ( $\varepsilon_2 = -0.20$ ), where the value of the limit strain surpasses the strain path  $\rho = -0.5$ , followed by the  $0^\circ$  direction ( $\varepsilon_2 = -0.15$ ) and finally by the  $45^\circ$  direction ( $\varepsilon_2 = -0.1$ ), whereby both the  $0^\circ$  and  $45^\circ$  directions do not reach the strain path  $\rho = -0.5$ .

The three FLCs show a tendency to decrease the limit strain values from the US condition until the PS condition is reached (left-hand side of the FLC), forming an approximately straight line. In the PS condition, the lowest values of the three FLCs can be observed, where none of the results yielded values of null minor strain. In the case of major strain, the highest value is observed for the  $0^\circ$  ( $\varepsilon_1 = 0.21$ ) direction, followed by both the  $45^\circ$  and  $90^\circ$  directions ( $\varepsilon_1 = 0.20$ ). On the right-hand side of

the FLD, where the limit strain can be seen from the PS condition until the BS condition is reached, the three curves show a parabolic trend. The curves with the higher limit values are those for the  $0^\circ$  and  $45^\circ$  directions, and the lowest curve is observed for the  $90^\circ$  direction. In the BS condition, the limit strain values of the three curves are very similar and very close to the strain path  $\rho = 1$ . Generally, the highest values are obtained in the US condition, and the lowest values are obtained in the PS condition.

### 3.3. Strain Paths

**Figure 1d** shows the strain values and strain path in the  $0^\circ$  direction corresponding to the samples with strain percentages and effective strains shown in **Table 4**. The highest value indicated in each strain path is the limit strain in US (gray circle), PS (black diamond), and BS (white squares). The different strain paths were fit by a second-order line with an  $R^2$  value very close to

**Table 4.** Analysis of the principal strain values ( $\varepsilon_1$ ,  $\varepsilon_2$ ,  $\varepsilon_{\text{eff}}$ ) of different strain paths.

	US			PS			BS		
	$\varepsilon_1$	$\varepsilon_2$	$\varepsilon_{\text{eff}}$	$\varepsilon_1$	$\varepsilon_2$	$\varepsilon_{\text{eff}}$	$\varepsilon_1$	$\varepsilon_2$	$\varepsilon_{\text{eff}}$
Initial material	0	0	0	0	0	0	0	0	0
Low strain	0.06	-0.02	0.06	0.01	-0.001	0.01	0.02	0.01	0.03
High strain	0.27	-0.11	0.27	0.06	-0.008	0.07	0.13	0.10	0.23
Limit strain	0.37	-0.15	0.37	0.23	-0.03	0.25	0.24	0.23	0.47

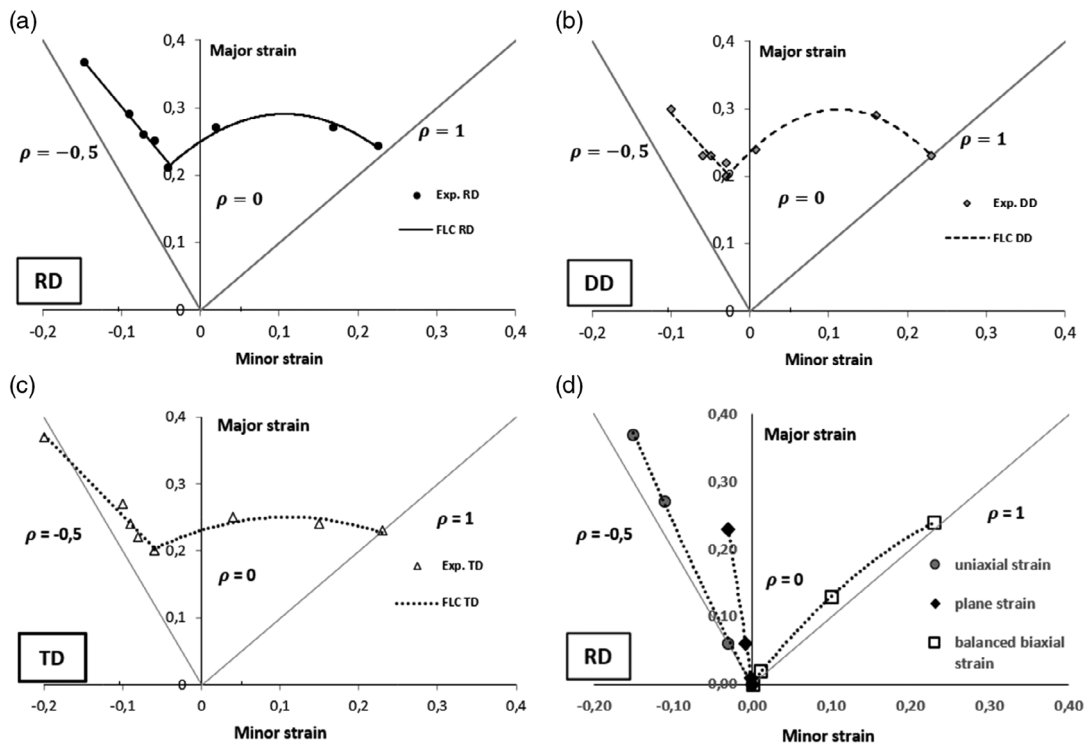


**Figure 1.** Experimental FLD AISI 430 stainless steel studied by performing a Marciniak test for a) the RD (black circles), b) diagonal to the RD (gray rhombuses), and c) transverse to the RD (white triangles) and d) strain paths to US (gray circles), PS (black rhombuses), and BS (white squares).

1. The US path shows that the values begin to separate from the ratio  $\rho = -0.5$ , exhibiting curvature from the beginning of the strain until the limit strain value is reached. The PS path shows that the values begin to separate from the null value, exhibiting a fairly linear strain path from the beginning of the strain until the limit strain value is reached. In the case of the BS path, the strain values depart from the ratio  $\rho = 1$ . However, the strain path reaches a limit strain value very close to  $\rho = 1$ , exhibiting curvature from the beginning of the strain until the limit strain value is reached.

### 3.4. EBSD

Figure 2a–g shows an EBSD-based inverse pole (IP) figure of the studied steel. In Figure 2a, the measurement of initial material revealed a nonhomogeneous grain size with an average grain size of  $\approx 21 \mu\text{m}$ . Figure 2b,d,f, corresponding to US, PS, and BS paths to low strain level, respectively, does not show a predominance of orientation, except in Figure 2f, where a slight increase of grains with  $\{001\}$  orientation can be seen. In Figure 2c, corresponding to US at high strain level, it is possible to distinguish an elongation of the grains induced by strain. The grain orientation does not show a marked trend on the orientation changes. Figure 2e corresponding to PS at a high strain level shows a great similarity for both grain orientation and grain shape compared with the grain orientation and grain shape for both initial material and low strain level. The changes most relevant are shown in Figure 2g corresponding to balanced BS at high strain level. Clearly, a significant change on the grain orientation can be observed, which shows changes toward  $\{001\}$  and  $\{111\}$  orientations.

### 3.5. Texture Evolution

Figure 3 shows the ODF of the initial material and the two strain levels of US, PS, and BS in the RD direction of the samples (experimental and numerical simulation to high strain). In Figure 3a, the ideal positions of the most important BCC rolling texture components in the  $\varphi_2 = 45^\circ$  section of the Euler space are shown. The texture analysis of the initial material (undeformed) is shown in Figure 3b. The strongest intensities are near the  $\{554\} \langle 225 \rangle$  component with  $\approx 2.8$  multiple of random density (mrd), followed by the  $\{001\} \langle 010 \rangle$  and the  $\{001\} \langle 110 \rangle$  components with  $\approx 2.2$  mrd. Figure 3c shows that after US is applied to  $\varepsilon_1 = 0.06$  and  $\varepsilon_2 = -0.02$ , the  $\{113\} \langle 110 \rangle$  component intensifies (from  $\approx 3.1$  to  $\approx 6.3$  mrd), the near- $\{001\} \langle 110 \rangle$  component slightly decreases (from  $\approx 2.5$  to  $\approx 2$  mrd), and the intensity peak of the  $\{554\} \langle 225 \rangle$  component slightly weakens (from  $\approx 3.9$  to  $\approx 3.2$  mrd) and widens.

Figure 3d shows the texture after applying US to  $\varepsilon_1 = 0.27$  and  $\varepsilon_2 = -0.11$ ; the  $\{113\} \langle 110 \rangle$  component shows a decrease in intensity, while the  $\{001\} \langle 110 \rangle$  and  $\{554\} \langle 225 \rangle$  components do not exhibit significant changes. In Figure 3e, drastic decreases in the  $\{001\} \langle 110 \rangle$  and  $\{001\} \langle 010 \rangle$  components can be observed after applying PS compression to  $\varepsilon_1 = 0.01$  and  $\varepsilon_2 = -0.001$ . The ODF of Figure 3f corresponding to PS with  $\varepsilon_1 = 0.06$  and  $\varepsilon_2 = -0.008$  shows intense peaks close to the  $\{001\} \langle 010 \rangle$  component together with a low-intensity peak for the  $\{001\} \langle 110 \rangle$  component. Figure 3g shows the texture

measured after BS with  $\varepsilon_1 = 0.02$  and  $\varepsilon_2 = -0.01$ ; with respect to the initial material, it shows an increase in the intensity of the  $\{001\} \langle 010 \rangle$  component with  $\approx 6.2$  mrd and a decrease in the intensity of the  $\{554\} \langle 225 \rangle$  component with  $\approx 3.2$  mrd. The strongest changes can be seen for the texture of Figure 3h observed after applying a BS of  $\varepsilon_1 = 0.13$  and  $\varepsilon_2 = -0.10$ , exhibiting an increase in components that constitute the  $\gamma$  fiber and an increase in both the  $\{001\} \langle 010 \rangle$  and  $\{001\} \langle 110 \rangle$  components, all of which have an intensity of  $\approx 5$  mrd.

### 3.6. Texture Simulation

Figure 4 shows the initial starting texture (Figure 4a), together with the ODFs, of the deformed samples after uniaxial, PS, and BS tests, which were simulated by the FCT crystal plasticity model. In most cases, in the different strain paths, the simulated intensities are very similar to the experimental texture components. For the uniaxially strained sample, as shown in Figure 4b, a low concentration of intensity close to the cube ideal component and a decrease in the  $\{554\} \langle 225 \rangle$  and an increase in the  $\{hkl\} \langle 110 \rangle$  components could be observed. In Figure 4c, corresponding to PS compression, a strong  $\{554\} \langle 225 \rangle$  component is observed and is similar to the experimental component; the presence of the  $\{111\} \langle 110 \rangle$  component is also observed. Furthermore, a decrease in  $\{hkl\} \langle 110 \rangle$  components and near absence of cube and rotated cube components can be observed. Similar to the experimental results in Figure 4d, the simulation of BS can be observed, whereby the most marked texture components are close to the  $\{111\} \langle uvw \rangle$ ,  $\{554\} \langle 225 \rangle$ , and  $\{001\} \langle 100 \rangle$  components in both the experiment and simulations. Clearly, there is good qualitative agreement for most of the simulated textures, particularly for BS conditions. However, the most similar simulated texture, both qualitative and quantitative, is the initial texture.

### 3.7. The Evolution of Fiber Textures

Figure 5b–h shows that during the tests, both the  $\alpha$  and  $\gamma$  fibers show different behaviors in the US, PS, and BS paths. In the case of the US condition with  $\varepsilon_1 = 0.06$  and  $\varepsilon_2 = -0.02$  (Figure 5c) and  $\varepsilon_1 = 0.27$  and  $\varepsilon_2 = -0.11$  (Figure 5d), the  $\gamma$  fiber does not show significant changes in any of the three states. In contrast, the texture intensities of the  $\alpha$  fiber exhibit an increase near the  $\{113\} \langle 110 \rangle$ ,  $\{112\} \langle 110 \rangle$ , and  $\{223\} \langle 110 \rangle$  components with  $\varepsilon_1 = 0.06$  and  $\varepsilon_2 = -0.02$ , while with  $\varepsilon_1 = 0.27$  and  $\varepsilon_2 = -0.11$ ,  $\alpha$  fiber shows a decrease. In the case of PS with  $\varepsilon_1 = 0.01$  and  $\varepsilon_2 = -0.001$  (Figure 5e) or with  $\varepsilon_1 = 0.06$  and  $\varepsilon_2 = -0.008$  (Figure 5f), the intensity of the  $\gamma$  fiber shows slight changes, specifically near the  $\{111\} \langle 110 \rangle$  components of the three states (undeformed, low strain, and high strain). In the same way, the  $\alpha$  fiber shows various changes in intensity in most of the  $\{hkl\} \langle 110 \rangle$  fiber components, with  $\varepsilon_1 = 0.01$  and  $\varepsilon_2 = -0.001$  and an increase to  $\varepsilon_1 = 0.06$  and  $\varepsilon_2 = -0.008$ , specifically for the  $\{001\} \langle 110 \rangle$  and  $\{111\} \langle 110 \rangle$  components. The  $\gamma$  fiber after strain with  $\varepsilon_1 = 0.02$  and  $\varepsilon_2 = 0.01$  does not show significant changes, but with  $\varepsilon_1 = 0.13$  and  $\varepsilon_2 = 0.10$ , a significant increase can be observed for the main components.

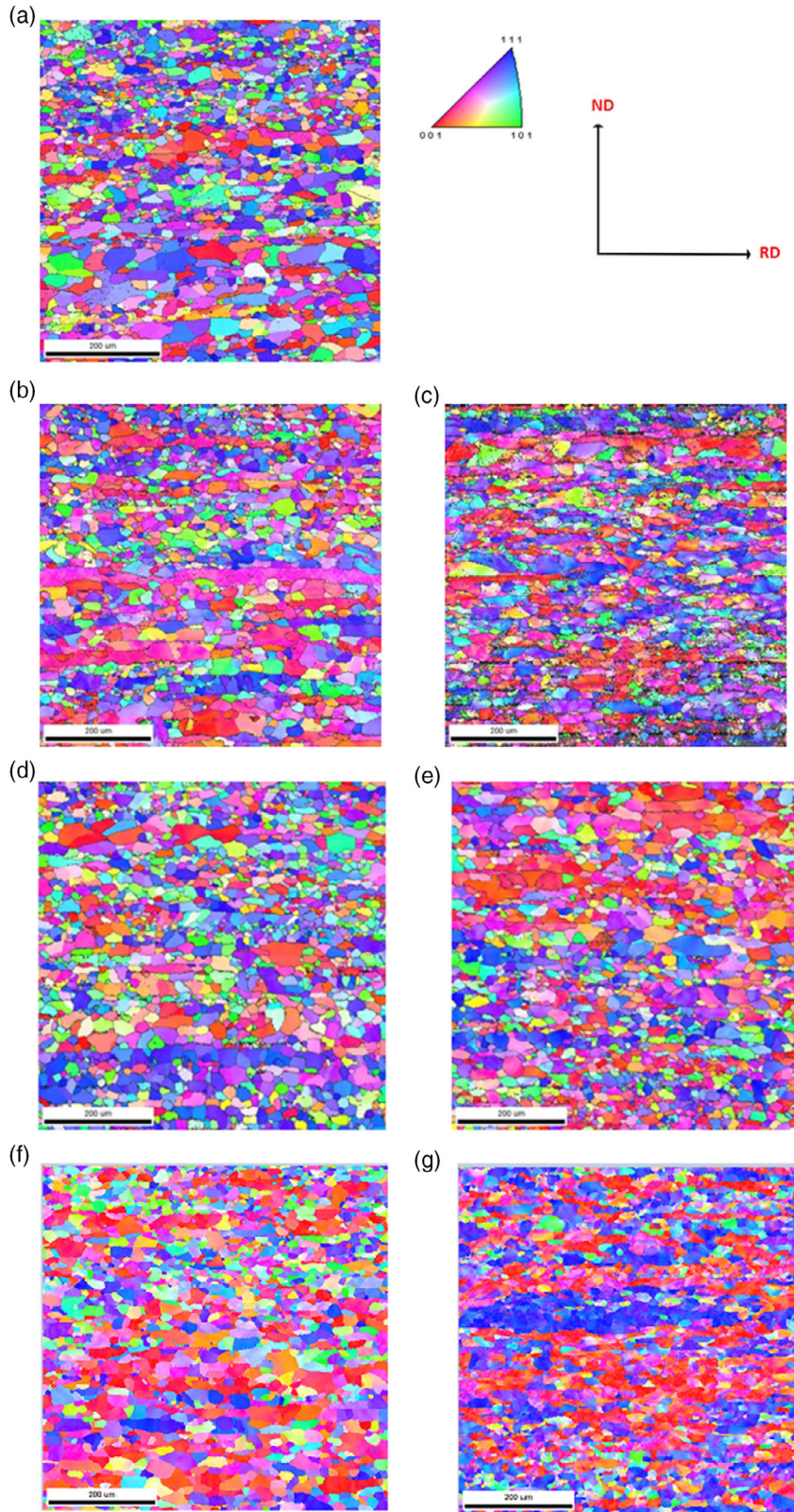


**Figure 2.** ND IP figure maps observed after different strain levels and different strain paths. a) Initial material, US with b) low strain and c) high strain, PS with d) low and e) high strain level, and balanced BS f) low strain and g) high strain. The color code corresponds to the legend next to (a).

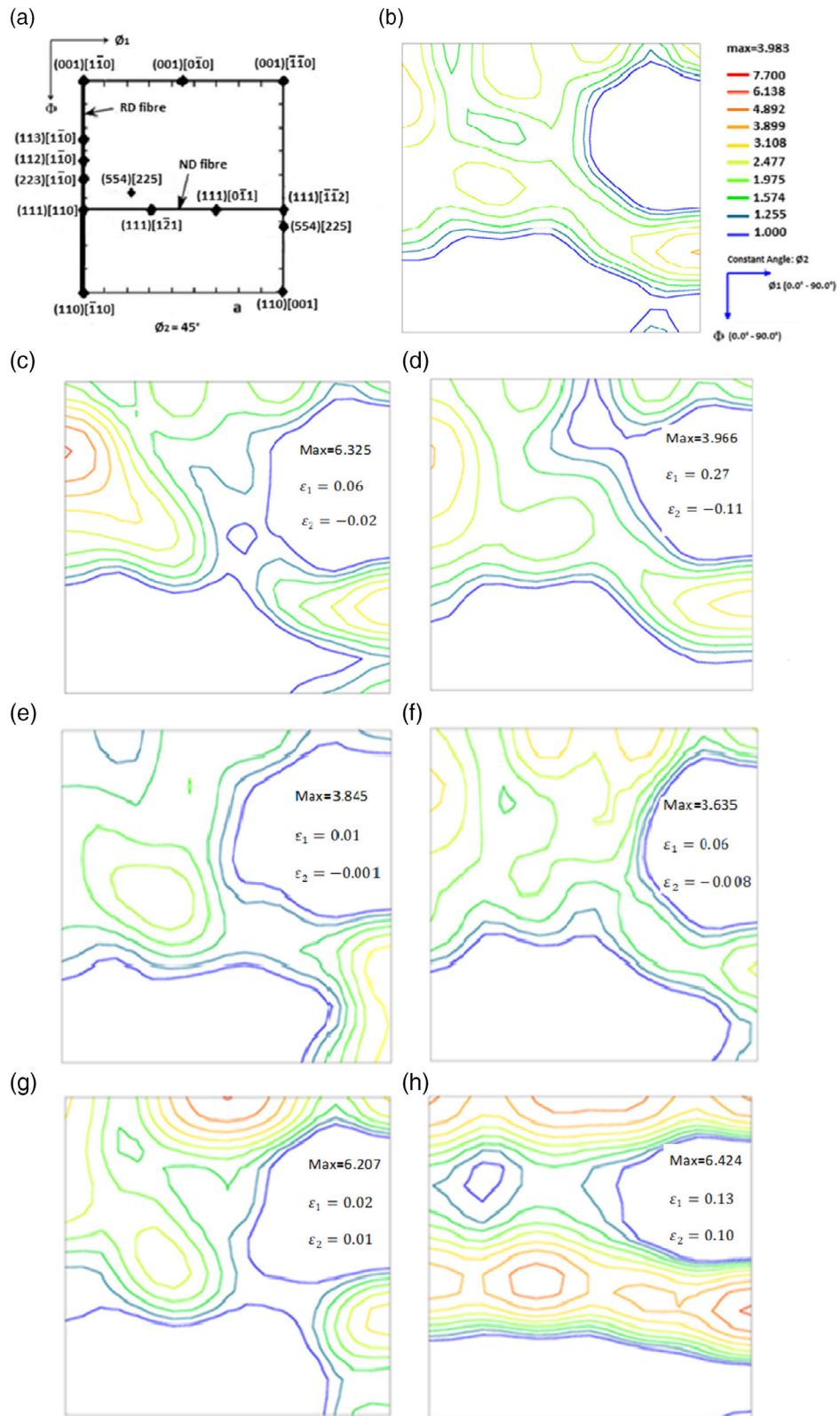


**Figure 3.** a) Ideal positions of the most important BCC rolling texture components in the  $\phi_2 = 45^\circ$  section of the Euler space.  $\phi_2 = 45^\circ$  section of the ODF of the (b) initial texture (undeformed), (c) US to low strain, (d) US to high strain, (e) PS to low strain, (f) PS to high strain, (g) BS to low strain, and (h) BS to high strain.



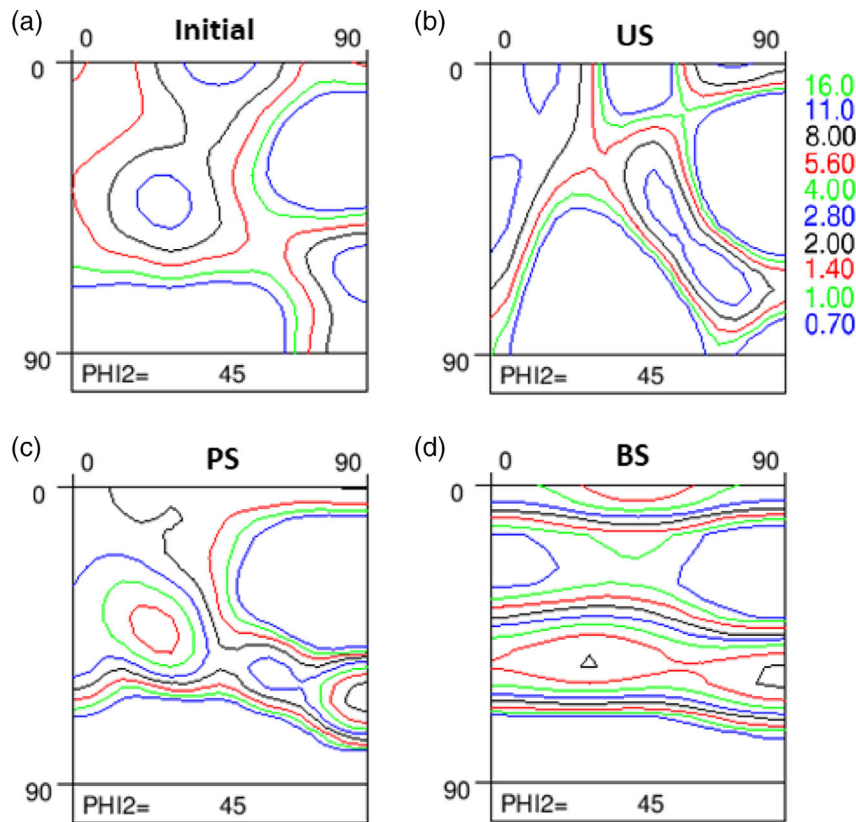


**Figure 4.** a) Numerical simulation of the initial texture, b) numerical simulation of the texture at high strain by US ( $\epsilon_1 = 0.27$ ,  $\epsilon_2 = -0.11$ ), c) numerical simulation of the texture at high strain by PS ( $\epsilon_1 = 0.06$ ,  $\epsilon_2 = -0.008$ ), and d) numerical simulation of the texture at high strain by BS ( $\epsilon_1 = 0.13$ ,  $\epsilon_2 = -0.10$ ).

### 3.8. The Evolution of Grain Boundary Misorientation

Figure 4 shows the angular grain boundary misorientation of the initial material (undeformed material) for both low- and high-strained materials. In Figure 4a, the grain boundary misorientation under US shows that the low-angle grain boundaries (LAGBs) tend to increase the number fraction to low strain, and the high-angle grain boundaries (HAGBs) tend to decrease the number fraction. At high strain, the LAGBs show a trend of decreasing the number fraction, and the HAGBs do not show significant changes. For PS, as shown in Figure 4b, at low strain, the LAGBs show a tendency to increase the number fraction, but the LAGBs show a tendency to decrease. At high strains, both low and high grain boundaries initially return. For BS, Figure 4c, at low strain, neither LAGBs, nor HAGBs show a significant change; however, at high strain, the LAGBs tend to increase, and the HAGBs tend to decrease.

## 4. Discussion

### 4.1. Formability and Strain Path

Figure 1a–c shows that for the limit strain values corresponding to US, the highest values obtained with major strain correspond to the  $0^\circ$  and  $90^\circ$  directions (Figure 1a,c), and the lowest value

corresponds to the  $45^\circ$  direction (Figure 1b). It was theoretically expected that the major strain values would reach approximately two times the coefficient of the strain hardening exponent ( $n$ ),<sup>[26]</sup> for which the experimental results in the  $0^\circ$  and  $90^\circ$  directions were reached. However, in the  $45^\circ$  direction, the limit strain value is low at  $\approx 17\%$ . This may be due to the low  $R$ -value given that under US conditions, the minor limit strain values move to the right or left of the strain path  $\rho = -0.5$  (continuous gray line) depending on whether its value is less or larger than 1. The  $n$ -values and  $R$ -values corresponding to each direction are shown in Table 2 and 3, respectively. The limit strain values correspond to minor strain; the highest value is at  $90^\circ$ , followed by  $0^\circ$ , and the lowest value corresponds to  $45^\circ$ . As previously mentioned, the minor strain is directly influenced by the  $R$ -value, whereby it is displaced to the left of the strain path  $\rho = -0.5$  (gray line) for an  $R$ -value  $> 1$  and displaced to the right when the  $R$ -value  $< 1$ .<sup>[26]</sup> The experimental results of the minor limit strain show good agreement with the  $R$ -value, as shown in Figure 1a–c.

The coefficient of the strain hardening value in the  $45^\circ$  direction is  $n = 0.18$ , and the limit strain value is 17%, where the limit strain should be close to two times the coefficient of the strain hardening value ( $n$ ). This could be attributed to the fact that necking was caused by the maximum minor strain, which was allowed due to the low  $R$ -value ( $R = 0.58$ ). For the limit strain values corresponding to the PS condition, the highest value obtained with major strain corresponds to  $0^\circ$ , and the lowest

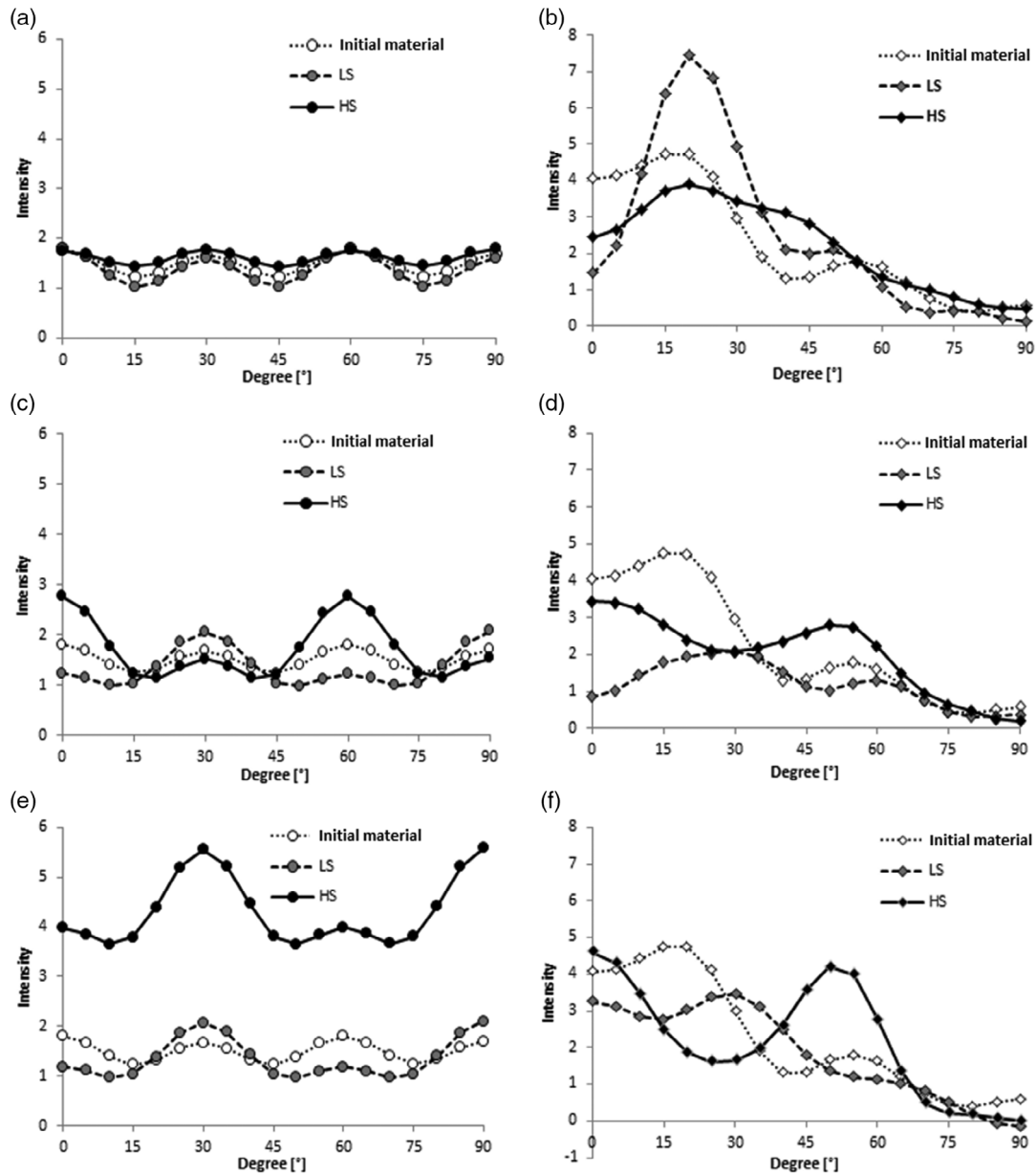


**Figure 5.** Evolution of the a) initial, low strain, and high strain of  $\gamma$  fibers in the US condition, b) initial, low strain, and high strain of  $\alpha$  fibers in the US condition, c) initial, low strain, and high strain of  $\gamma$  fibers in the PS condition, d) initial, low strain, and high strain of  $\alpha$  fibers in the PS condition, e) initial, low strain, and high strain of  $\gamma$  fibers in the BS condition, and f) initial, low strain, and high strain of  $\alpha$  fibers in the BS condition.

values correspond to  $45^\circ$  and  $90^\circ$ , with a very small difference. In the same way as was observed under US conditions, it was theoretically expected that the major limit strain value would reach approximately  $n$  and that the minor limit strain would be 0. In the case of the PS condition, the major limit strain values are very similar and close to the coefficient of the strain hardening value. Some authors have reported that when the strain rate sensitivity coefficient ( $m$ ) is high, the major limit strain in the PS condition is larger than the coefficient  $n$ .<sup>[26,44]</sup> This could be the cause of the small increase in the major strain. The limit strain values correspond to minor strain; the highest value is obtained at  $90^\circ$ , and the lowest value corresponds to  $0^\circ$  and  $45^\circ$ . Theoretically, the

minor limit strain should be zero. The experimental results show that FLCs under PS conditions did not yield minor limit strain values of null. This may be caused by the geometry of the samples on the strain path. We further discuss this particular issue in the next section. On the right-hand side of the FLD, the three curves ( $0^\circ$ ,  $45^\circ$ , and  $90^\circ$ ) show a parabolic trend. The highest values are shown by the  $45^\circ$  curve followed by the  $0^\circ$  curve, and the lowest values are shown by the  $90^\circ$  curve. This cannot be related to any mechanical property. Some authors argue that a high value of normal anisotropy decreases the limit strain values on the right side of the FLD<sup>[26,44]</sup> and mention in numerical simulation analysis that high  $R$ -values decrease the limit strain values on the

right-hand side of the FLD. However, this is unrealistic because the model used does not involve sheet materials with internal defects. In contrast, Bhargava et al.<sup>[45]</sup> mentioned that this increase can be attributed to an increase in  $\gamma$  fibers. It is interesting to observe in Figure 1a–c that the BS values of the three limit strains are very similar, yet not the same. The latter is attributed to the fact that the biaxial load is the same and independent in all directions in the sample.

## 4.2. Influence of Texture on Strain Path

### 4.2.1. Strain Path-Related Texture Evolution

In Figure 1d, the strain path under US is a straight line with a weak tendency toward a second-order line. In the PS path, the experimental points follow a straight line, whereas under BS, similar to the US path, a straight line with a weak tendency toward a second-order line is observed. The curves indicate that the experimental tests were carried out correctly as there are no abrupt changes in strain paths.<sup>[29]</sup>

### 4.2.2. Uniaxial Strain

In the US path condition, comparing Figure 3b–d shows that there are no significant changes in texture, except for a concentration of textures close to the  $\{113\} \langle 110 \rangle$  ideal component with a maximum mrd of  $\approx 6.3$ , at  $\epsilon_1 = 0.06$  and  $\epsilon_2 = -0.02$ . An increase in this component could cause a shift to the right from the ideal strain path ( $\rho = -0.5$ , left gray straight line) due to a decrease in the overall  $R$ -value produced by the appearance of this component, as was reported by Ray et al.<sup>[35]</sup> It is interesting to note that none of the components of the  $\gamma$  fiber show significant changes in intensity in any of the three US states (undeformed, low strain, and high strain), indicating that the  $\gamma$  fiber has no influence on the strain path. In case of the  $\alpha$  fiber, changes in intensity can be observed in the different components of the fiber close to the  $\{hkl\} \langle 110 \rangle$  components. These variations could be related to the slight shift from the reference line of the strain path  $\rho = -0.5$  toward the right side, causing the curvature of the strain path.

### 4.2.3. Plane Strain

Under PS conditions, Figure 3b,e,f does not show significant changes in the texture components. The maximum intensity was observed in the undeformed condition, decreasing the intensities under low- and high-strain conditions. Note that the maximum intensities are very similar in the three stages, and the slight variations in orientation could be due to the low strain levels in the plain strain path ( $\epsilon_1 = 0.01$  and  $\epsilon_2 = -0.001$ ;  $\epsilon_1 = 0.06$  and  $\epsilon_2 = -0.008$ ). In the case of  $\gamma$  and  $\alpha$  fibers, slight changes can be observed in different components. These changes do not show a clear trend after straining; therefore, it is not possible to attribute these fiber changes to the behavior of the PS path condition.

### 4.2.4. Biaxial Strain

Under BS path conditions, changes in texture were observed. Figure 3g denotes a sharp maximum of both cube components  $\{001\} \langle 010 \rangle$  with  $\approx 6$  mrd and  $\{554\} \langle 225 \rangle$  component with  $\approx 5$  mrd. Figure 1b shows that there is a clear tendency for the path to start moving to the left of the reference strain path  $\rho = 1$  (right gray straight line) despite the biaxial deformation path. This may be due to changes in texture intensities between the two stages (undeformed and low strain). In the case of high strain, Figure 3h clearly shows a concentration of  $\{111\} \langle uvw \rangle$  and  $\{554\} \langle 225 \rangle$  rotated cube components and a spread of components close to the ideal cube component. It is known that the formability progressively decreases when the volume fraction of the ideal cube orientation increases.<sup>[36]</sup> Furthermore, it has also been established that the  $\gamma$  fiber developed during deformation improves the formability behavior.<sup>[46]</sup> As shown in Figure 3h, a high BS increase in the  $\gamma$  fiber was observed. In the case of the  $\alpha$  fiber at  $\epsilon_1 = 0.02$  and  $\epsilon_2 = 0.01$  and at  $\epsilon_1 = 0.13$  and  $\epsilon_2 = 0.10$ , the fiber does not show any clear development that can be used to identify the tendency of the strain path in biaxial conditions. In contrast, for  $\gamma$  fibers, an increase in the number of  $\alpha$  fibers decreases the formability properties.<sup>[46]</sup>

In summary, the relationship among the evolution of microstructural, mechanical, and formability properties can be described as follows:

The curvature of the US path is due to the fact that the texture (predominantly  $\gamma$  fiber) does not show significant change neither at low strain, nor at high strain. Only slight changes can be observed in Figure 3b,c and 5a,b. In contrast, the  $\alpha$  fiber shows an increase in volume fraction, which is the prime cause of the decrease in  $R$ -value and for the same reason a trend of strain path curvature to move away to the right of the ratio  $\rho = -0.5$ . It should be noted that the reorientation of the grains resulted in a significant increase near the component  $\{113\} \langle 110 \rangle$  at low strain. This increase is the main cause of the decrease in the  $R$ -value and, therefore, the cause of the tendency to move away to the right of the ratio  $\rho = -0.5$ .

The trend observed in the evolution of the PS is due to the limited change of the crystallographic texture. The intensities in the undeformed material and at the two strain levels are similar, which eventually leads to the straight path in PS.

The balanced BS path is clearly a second-order line. This trend is, obviously, a consequence of the different texture component intensities developed during the deformation process. It is interesting to observe that at the low strain level, even though the applied load is balanced, the strain path shows a trend to move away to the left of the ratio  $\rho = 1$ . This is a consequence of the development of the cube component of which intensity reaches a value of  $\approx 6.2$  mrd with a near-null variation of the  $\gamma$  fiber components and a slight variation of  $\alpha$  fiber components. During the deformation process from low strain to high strain, a decrease of the cube component can be observed and an increase of the  $\gamma$  fiber component, whereby the strain path tends to the ratio  $\rho = 1$ . This trend could be related with the development of the  $\gamma$  fiber components.

#### 4.2.5. Fiber Evolution

The  $\gamma$  fiber remains almost constant under US and PS conditions, both with slight variations. It is important to note that under US and PS conditions, there is a small spreading of components toward the  $\gamma$  fiber, although the variations in intensity are low. These changes can be seen as slightly more noticeable in the PS condition by considering that the effective strain levels are low in both states, 0.01 and 0.07 (see Table 4), compared with those in the other strain paths. The strain path with a linear trend under both conditions (uniaxial and plane) could be attributed to the slight changes in intensity of each component. In the case of BS conditions, the variation in the  $\gamma$  fiber is evidently greater as the amount of effective strain increases. In the case of the  $\alpha$  fiber, changes in intensity can be observed in different components of the fiber in the three strain paths. However, a clear trend related to the strain is not defined, as in the case of  $\gamma$  fibers.

#### 4.3. Simulated Texture

The evolution of the crystallographic texture was calculated using the FCT model. The simulated texture components show general qualitative agreement with the experimental results for the three strain paths; however, small differences in the intensities of some components can be seen.

By comparing the experimental and simulation textures, the following can be observed: in Figure 4b, the experimental components with the highest intensities are  $\{554\} \langle 225 \rangle$  with 3.9 mrd and  $\{113\} \langle 110 \rangle$  with 3.1 mrd. In Figure 4a, the simulated intensities of the  $\{554\} \langle 225 \rangle$  and  $\{113\} \langle 110 \rangle$  components are 2.8 and 1.4 mrd, respectively. In the same way, both cube and rotated cube components have, experimentally, higher intensities than the simulated components. The ODFs in Figure 4 show the smooth rotation of the grains of the cube component in the direction of the rotated cube components. Figure 3 and 4 show the experimental and simulated texture components, respectively, with US, PS, and BS applied at high strain levels. As previously mentioned in Section 3.5, qualitatively, the simulated texture has a good approximation for the different components; however, there are small differences. Clearly, the presence of grains with both orientations close to  $\{113\} \langle 110 \rangle$  and cubic components in the experimental texture can be seen (Figure 4d); in contrast, these grains cannot be seen in the simulated textures (Figure 4b). A similar description of the US path can be seen in the PS path, where the presence of grains with both orientations close to  $\{113\} \langle 110 \rangle$  and cubic components can be observed. The most similar results between both the experimental and the simulated textures are shown in Figure 3h and 4d, corresponding to BS at high strain levels. In quantitative terms, differences can be observed in the three strain paths; however, in qualitative terms, the observed components, both experimental and simulated, are very similar. In general, the intensities of the simulated texture components are higher than the experimental intensities.

Differences between the experimental and simulation results could be attributed to the specific constraints of the model. First, the interaction between neighboring grains was not considered,<sup>[47]</sup> and this condition could influence the internal stresses between neighboring grains. Internal stresses affect texture

development in terms of quantitative deviations, such as the rotation rate and texture intensities, and qualitative deviations, such as stable orientations, are not considered.<sup>[34]</sup> Furthermore, the absence of components such as those close to  $\{113\} \langle 110 \rangle$  and cube components are attributed to their initial simulated textures.

#### 4.4. Evolution of Grain Misorientation

The low-angle ( $\leq 15^\circ$ ) misorientation distribution comes from the contribution of dislocation accumulation, whereas the high-angle

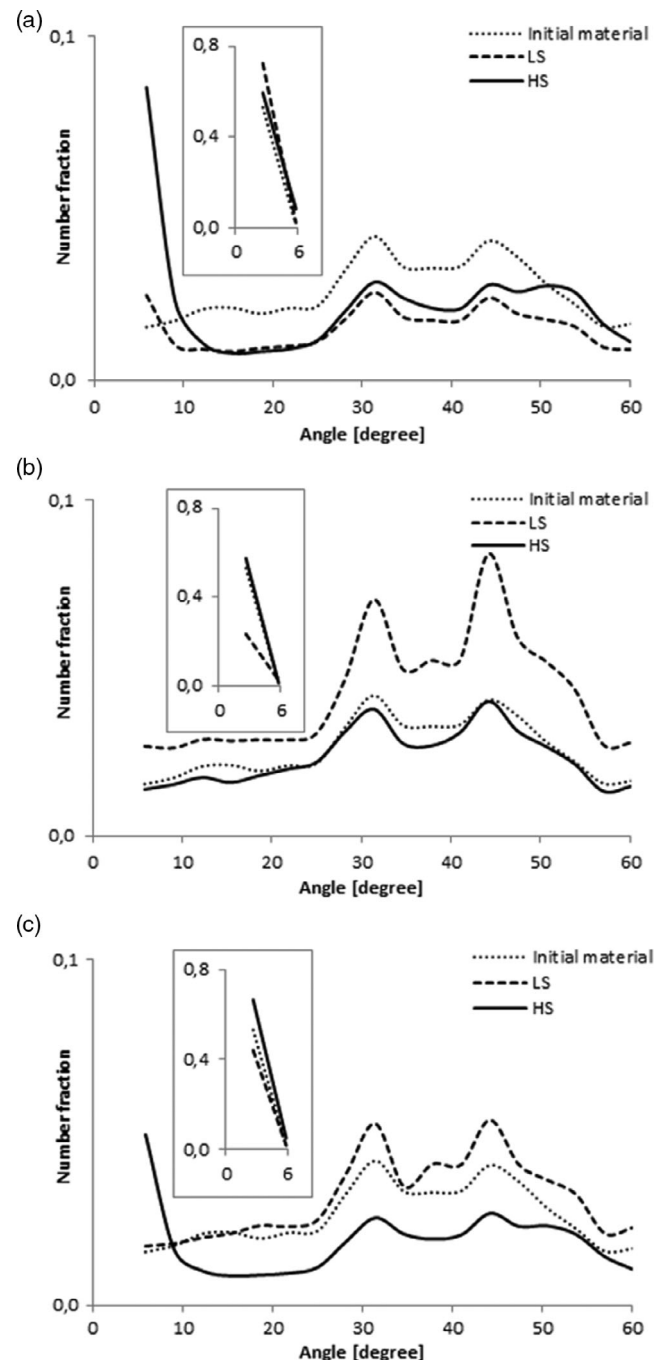


**Figure 6.** Grain boundary misorientation with a) US, b) PS, and c) BS.

( $\geq 40^\circ$ ) distribution is attributed to texture evolution during deformation.<sup>[45,48]</sup> Figure 6 shows that the grain misorientation of the initial material has a larger fraction of low-angle boundaries, which could be caused by the existing residual deformations produced in the skin-pass rolling process. In the three strain paths (Figure 6a,b,c), the fraction of HAGBs decrease with increasing strain, and they form LAGBs. The behavior of the LAGB and HAGB misorientations has a direct relationship with the effective strain levels. The higher the effective strain, the greater the dislocation density and the formation of LAGBs. In contrast, there was an increase in the distribution of grain boundary misorientations at low strain levels. In Figure 6a, the fraction of LAGBs increases, in contrast to what is indicated by the literature.<sup>[48]</sup> The increase in the fraction of LAGBs at low strain could be correlated with the increase in texture intensity. Figure 6b shows that the fraction of HAGBs increases. Note that HAGB formation caused by high strain could be thought of as an energy-storage mechanism.<sup>[49]</sup> The literature only reports results on high PS<sup>[48]</sup> that cannot be compared with the former dataset under low strain. Similar misorientation behavior was observed for the BS path.

## 5. Conclusion

A thorough formability and microstructural analysis of an AISI 430 stainless steel was performed. The microstructure analysis revealed a single-phase ferritic structure with a heterogeneous size distribution and average grain diameter of  $\approx 21 \mu\text{m}$ . The texture analysis showed the predominance of  $\{100\} \langle 100 \rangle$  cube,  $\{001\} \langle 110 \rangle$  rotated cube, and  $\{554\} \langle 225 \rangle$  texture components.

Experimental formability for FSS AISI 430 sheets was evaluated. The following conclusions were obtained.

The studied material showed a capacity to withstand plastic strain before the onset of necking within standard ranges. Limit strain values reasonably correlates with both strain hardening exponent, in the case of major strain value and for the minor strain values, with  $R$ -value.

The analyzed strain paths showed a slight trend to a second-order line in the case of uniaxial and BS paths. This deviation from linearity is attributed purely to the evolution of  $R$ -value whose crystallographic texture is predominantly  $\alpha$  fiber  $\{hkl\} \langle 110 \rangle$  for US paths. For the BS path, a second-order line with a trend to the balanced BS is observed. This is clearly a consequence of the increase in  $\gamma$  fiber  $\{111\} \langle uvw \rangle$ . The PS path shows a trend to a first-order line. This is due to the negligible crystallographic texture changes.

The evolution of grain boundary misorientations shows a mixed behavior for different strain paths. LAGB fraction increases markedly in both PS and BS paths, whereas HAGB misorientations represent a small contribution in US path.

The texture evolution determined via the FCT model shows a good qualitative agreement with the experimental results under high strains. The simulations reproduce well the intensity maxima in all three strain paths.

## Acknowledgements

The authors are pleased to acknowledge the support of the Universidad de Santiago de Chile through their USA1899 project (postdoctoral program)

in the Metallurgical Engineering Department. E.I. H-D acknowledges the support of the National Agency for Research and Development (ANID-Chile)/Doctorado Nacional/2017-21171319.

## Conflict of Interest

The authors declare no conflict of interest.

## Data Availability Statement

Research data are not shared.

## Keywords

formability, microstructure, stainless steel, strain paths, texture

Received: February 23, 2021

Revised: October 19, 2021

Published online: November 10, 2021

- [1] P. Snelgrove, *Stainless steel automotive and transport developments*. *Int. Stainl. Steel Forum [Internet]*, **2016**, pp. 1–5, <http://www.worldstainless.org/library/>.
- [2] H.-R. Wang, Z. Xiao, J. Qu, H.-W. Yang, Z.-Y. Cao, X. Guo, *J. Iron Steel Res. Int.* **2013**, *20*, 75.
- [3] M. A. Meyers, K. K. Chawla, *Mechanical Behavior of Materials*, Cambridge university press **2008**.
- [4] J. Rösler, H. Harders, M. Bäker, *Mechanical Behaviour of Engineering Materials: Metals, Ceramics, Polymers, and Composites*, Springer Science & Business Media **2007**.
- [5] S. P. Keeler, W. A. Backofen, *ASM Trans. Q* **1963**, *56*, 25.
- [6] G. M. Goodwin, *SAE Trans.* **1968**, *77*, 380.
- [7] Z. Marciniak, K. Kuczyński, *Int. J. Mech. Sci.* **1967**, *9*, 609.
- [8] K. Nakazima, T. Kikuma, K. Hasuka, *Yawata Tech. Rep.* **1968**, *264*, 8517.
- [9] ISI, *Metallic Materials-Sheet and Strip Determination of Forming Limit Curves, Part 2: Determination of Forming Limit Curves in the Laboratory*, 12004-2:2008 ISI, International Organization for Standardization, Geneva **2008**, p. 33.
- [10] S. P. Keeler, *SAE Trans.* **1968**, *77*, 371.
- [11] R. Sowerby, E. Chu, J. L. Duncan, *Strains Metalforming* **1982**, *17*, 95.
- [12] A. Bragard, J. C. Baret, *Cent. Res. Metall.* **1972**, *33*, 53.
- [13] G. Marron, L. Moinier, P. Patou, J. Celeski, *A New Necking Criterion for the Forming Limit Diagrams*, Vol. 94, IDDRG, WG Meet, Haugesund **1997**, pp. 837–45.
- [14] P. Vacher, A. Haddad, R. Arrieux, *CIRP Ann. Manuf. Technol.* **1999**, *48*, 227.
- [15] W. Hotz, M. Merklein, A. Kuppert, H. Friebe, M. Klein, *Key Eng. Mater.* **2013**, *549*, 397.
- [16] J. Li, J. E. Carsley, T. B. Stoughton, L. G. Hector, S. J. Hu, *Int. J. Plast.* **2013**, *45*, 21.
- [17] A. J. Martínez-Donaire, F. J. García-Lomas, C. Vallengano, *Mater. Des.* **2014**, *57*, 135.
- [18] B. Eberle, W. Volk, in *7th Int. Conf. Work Numer Simul 3D Sheet Metal Form Process Numisheet 2008*, Interlaken, Switzerland **2008**, pp. 279–284.
- [19] W. Volk, P. Groche, A. Brosius, A. Ghiotti, B. L. Kinsey, M. Liewald, J. Yanagimoto, in *Models and modelling for process limits in metal forming*, CIRP Annals **2019**, *68*, pp. 775–798.
- [20] P. Hogström, J. W. Ringsberg, E. Johnson, *Int. J. Impact Eng.* **2009**, *36*, 1194.

- [21] K. Wang, J. E. Carsley, B. He, J. Li, L. Zhang, *J. Mater. Process. Technol.* **2014**, 214, 1120.
- [22] D. Morales-palma, C. Vallengano, F. J. García-lomas, *Mater. Des.* **2013**, 50, 798.
- [23] A. Abbas, G. Campoli, J. Sinke, R. Benedictus, *Mater. Des.* **2011**, 32, 1229.
- [24] D. Vysochinskiy, T. Coudert, O. S. Hopperstad, O. G. Lademo, A. Reyes, *J. Mater. Process. Technol.* **2016**, 227, 216.
- [25] R. A. Iquilio, F. M. Castro Cerda, A. Monsalve, C. F. Guzmán, S. J. Yanez, J. C. Pina, F. Vercruysse, R. H. Petrov, E. I. Saavedra, *Int. J. Mech. Sci.* **2019**, 153–154, 208.
- [26] J. Hu, Z. Marciniak, J. Duncan, (Eds.). *Mechanics of sheet metal forming*, Elsevier **2002**.
- [27] R. H. Wagoner, K. S. Chan, S. P. Keeler, *Forming Limit Diagrams: Concepts, Methods, and Applications*, Minerals, Metals and Material Society, Warrendale, PA **1989**, p. 343.
- [28] H. Conrad, *J. Mech. Work Technol.* **1978**, 2, 67.
- [29] A. Graf, W. F. Hosford, *Int. J. Mech. Sci.* **1994**, 36, 897.
- [30] M. Dilmeç, H. S. Halkacı, F. Oztürk, *Int. J. Adv. Manuf. Technol.* **2013**, 67, 2689.
- [31] A. Chenaoui, F. Sidoroff, A. Hihi, *J. Mech. Phys. Solids* **2000**, 48, 2559.
- [32] T. Hoc, S. Forest, *Int. J. Plast.* **2001**, 17, 65.
- [33] S. Flouriot, S. Forest, G. Cailletaud, A. Köster, L. Rémy, B. Burgardt, V. Gros, S. Mosset, J. Delautre, *Int. J. Fract.* **2003**, 124, 43.
- [34] D. Raabe, *Mater. Sci. Eng.: A* **1995**, 197, 31.
- [35] R. K. Ray, J. J. Jonas, R. E. Hook, *Cold rolling and annealing textures in low carbon and extra low carbon steels*, International materials reviews, **1994**, 39, 129.
- [36] P. D. Wu, S. R. Macewen, D. J. Lloyd, K. W. Neale, *Mater. Sci. Eng.: A* **2004**, 364, 182.
- [37] G. I. Taylor, *J. Inst. Met.* **1938**, 62, 307.
- [38] P. Van Houtte, E. Aernoudt, *Z. Met. Res. Adv. Tech.* **1975**, 66, 202.
- [39] J. J. Sidor, R. H. Petrov, L. A. I. Kestens, *Acta Mater.* **2011**, 59, 5735.
- [40] J. J. Sidor, K. Decroos, R. H. Petrov, L. A. I. Kestens, *Int. J. Plast.* **2015**, 66, 119.
- [41] L. S. Tóth, P. Van Houtte, *Textures Microstruct.* **1992**, 19, 229.
- [42] H. J. Bunge, R. A. Schwarzer, *Crystallographic texture and plastic anisotropy*, In Multiscale Modelling in Sheet Metal Forming Springer, Cham **2016**, pp. 47–78.
- [43] ASTM, *Standard Test Method for Plastic Strain Ratio  $r$  for Sheet Metal 1*, E517 A, ASTM, West Conshohocken, PA **1998**, pp. 1–8.
- [44] L. Zhang, J. Wang, *Int. J. Plast.* **2012**, 39, 103.
- [45] M. Bhargava, S. Chakrabarty, V. K. Barnwal, A. Tewari, S. K. Mishra, *Mater. Des.* **2018**, 152, 65.
- [46] B. Verlinden, J. Driver, I. Samajdar, R. D. Doherty, *Thermo-mechanical processing of metallic materials*, Elsevier **2007**.
- [47] P. Van Houtte, *Textures Microstruct.* **1988**, 8, 313.
- [48] D. A. Hughes, N. Hansen, *Acta Mater.* **1997**, 45, 3871.
- [49] A. L. Titchener, M. B. Bever, *Prog. Met. Phys.* **1958**, 7, 247.